

# Global three-dimensional draping of magnetic field lines in Earth's magnetosheath from in-situ spacecraft measurements

Bayane Michotte de Welle (✉ [bayane.michotte-de-welle@lpp.polytechnique.fr](mailto:bayane.michotte-de-welle@lpp.polytechnique.fr))

Université Paris-Saclay

Nicolas Aunai

CNRS

Gautier Nguyen

DGA

Benoit Lavraud

Research Institute in Astrophysics and Planetology

Vincent Génot

CNAP

Alexis Jeandet

CNRS

Roch Smets

Sorbonne Université

---

## Article

### Keywords:

**Posted Date:** April 22nd, 2022

**DOI:** <https://doi.org/10.21203/rs.3.rs-1514695/v1>

**License:**   This work is licensed under a Creative Commons Attribution 4.0 International License.

[Read Full License](#)

---

# Global three-dimensional draping of magnetic field lines in Earth's magnetosheath from in-situ spacecraft measurements

Bayane Michotte de Welle<sup>1</sup>, Nicolas Aunai<sup>1</sup>, Gautier Nguyen<sup>2</sup>, Benoit Lavraud<sup>3</sup>,  
Vincent Génot<sup>4</sup>, Alexis Jeandet<sup>1</sup>, Roch Smets<sup>1</sup>

<sup>1</sup> CNRS, Ecole polytechnique, Sorbonne Université, Univ Paris Sud, Observatoire de Paris, Institut Polytechnique de Paris, Université Paris-Saclay, PSL Research University, Laboratoire de Physique des Plasmas, Palaiseau, France

<sup>2</sup> Direction Générale de l'Armement, France

<sup>3</sup> Laboratoire d'Astrophysique de Bordeaux, Université Bordeaux, CNRS, Pessac, France

<sup>4</sup> Institut de Recherche en Astrophysique et Planétologie, CNRS, Université de Toulouse, CNES, Toulouse, France

April 13, 2022

**Magnetic field draping occurs when the magnetic field lines frozen in a plasma flow wrap around a body or plasma environment. The draping of the interplanetary magnetic field (IMF) around the Earth's magnetosphere has been confirmed in the early days of space exploration. However, its global and three-dimensional structure is known from modeling only, mostly numerical. Here, this structure in the dayside of the Earth's magnetosheath is determined as a function of the upstream IMF orientation purely from in-situ spacecraft observations. We show the draping structure can be organized in three distinct regimes depending on how radial the upstream IMF is. Quantitative analysis demonstrates how the draping pattern results from the frozen-in condition with the magnetosheath flow, deflected around the magnetopause.**

Magnetic field draping is a universal phenomenon in highly conducting magnetized astrophysical plasmas. It is known to occur around induced [8, 4] and intrinsic planetary magnetospheres ([9, 3, 17]), comets [37, 23], solar ejecta in the IMF [28, 12, 19], the heliosphere in the interstellar field [32, 35], galaxies in the intergalactic field [34]. Magnetic field draping is key in understanding how plasma environments couple with their surroundings. In particular it is of pivotal importance in determining the location, triggering and efficiency of magnetic reconnection at magnetic boundaries.

The closest example of magnetic field draping is found in the Earth's magnetosheath, where the IMF drapes around the magnetopause. This region thus constitutes an unique observatory for in-situ measurements of this ubiquitous plasma process. Predicted theoretically from the transport of field lines in gas dynamics models [46], the draping effect was first evidenced in the magnetosheath the following couple of years [9, 3] in spacecraft in-situ measurements, although very few data points were accessible at the time. Increasingly more detailed observations were subsequently performed [7, 31, 18, 16, 6, 24, 40], confirming the draping of the IMF and comparing the orientation of the magnetic field locally measured in the magnetosheath, to that predicted by models. Unfortunately, these observations were restricted to coarse angular sectors of the IMF orientations and to particular orbital planes. Our current understanding of how the magnetic field drapes around the magnetosphere in a global and three-dimensional manner and as a function of the IMF orientation thus only comes from analytical ([21, 15, 51]) and numerical modeling ([16, 49]). There is still so far no consistent equivalent from a purely observational standpoint.

An example of in-situ spacecraft data measured in the near-Earth environment, is given on Fig. 1a-d. The data shows the signatures typically seen in an outbound trajectory from the magnetosphere to the solar wind, going through the magnetosheath region. The magnetosphere is characterized by the strongest magnetic field amplitude, lowest density and most stagnant plasma of all three regions. The solar wind is easily recognized as a relatively dense plasma flowing at supersonic speed during the last part of the time interval. The magnetosheath is the region in between these two, downstream of the bow shock where the plasma is heated, compressed, and flows around the

obstacle after having been decelerated to a subsonic speed. In that region, the magnetic field increases in amplitude and drapes around the magnetopause.

Reconstructing the global and three-dimensional magnetic field draping pattern as a function of the IMF orientation, from such data, intrinsically local in space and time, is actually quite challenging. Firstly, the data is intrinsically heavily spatially biased by the satellite orbital planes. Reconstructing a global draping from observations thus imperiously requires having multiple spacecraft on significantly different orbits. Secondly, understanding the dependence of the draping on the IMF orientation requires the constant monitoring of the upstream solar wind from yet another spacecraft. And even if such data is available, estimating the causal IMF orientation for each magnetosheath measurement may come with possibly substantial errors that call for large statistics so that the errors do not dominate the results. Then, the magnetosheath flow carries many small scale plasma and magnetic fluctuations from which the macroscale field can only stand out if using again a large number of uncorrelated measurements. Unfortunately, the complexity of the time series makes it difficult to automatize the identification of time intervals during which the spacecraft explores regions of interest. Data selection is often performed manually, hampering large statistics, consequently adding substantial uncertainties when drawing conclusions. Last but not least is the fact that multivariate time series like that shown in Fig. 1 actually represent slices in an unsteady complex three-dimensional system in which the instantaneous position of the spacecraft relative to plasma structures is unknown. This space/time ambiguity substantially complicates the reconstruction of the spatial pattern of the draping, for which the magnetic field measured at a given time must be positioned relative to the magnetopause and bow shock boundaries.

All these difficulties can be overcome today. We indeed now have access to decades of in-situ measurements from a fleet of spacecraft that have been or still are exploring the near-Earth environment. Many of these missions have been operating at a time when solar wind monitoring was available. Furthermore, handling such a massive, heterogeneous and complex dataset to build large statistics is now within reach with the help of statistical learning. In this study, statistical learning was key to automatically detect all time intervals during which Cluster, Double Star, THEMIS and MMS spacecraft have measured magnetosheath data, as explained in the method section. This allowed us to gather the unprecedented number of 45 million magnetosheath in-situ measurements at 5 second resolution over a period of two decades, offering an excellent spatial coverage of the 3D dayside magnetosheath, under all and statistically unbiased IMF orientations (Figures 1f and g). Machine learning was also an asset in positioning each individual magnetosheath measurements relatively to the magnetopause and bow shock, by enabling the prediction of these boundaries' position given upstream solar wind/IMF parameters, as explained in the method section.

This work thus offers the first global and detailed three-dimensional reconstruction of the magnetic field draping around the magnetosphere, as a function of the IMF orientation. The observed draping patterns will be shown to be strongly and globally determined by the frozen-in condition in the deflected magnetosheath flow. To make this point clear, our reconstructed drapings are first presented in contrast to the one obtained from a widely used magnetostatic model [21] where no plasma is assumed, before quantitatively demonstrating the role of the frozen-in condition in the observed patterns. In the magnetostatic model, the potential magnetic field drapes between the bow shock boundary, where the normal component of the IMF is conserved, and the magnetopause boundary, to which the magnetic field is made tangential. Such draping is broadly used by researchers and has been at the root of studies of the dynamics of cosmic dust [14], spacecraft fine debris [13] and many other plasma processes occurring not only in the Earth's magnetosheath (e.g. [10]), but also in that of other planets such as Mercury [44, 43], Jupiter [27], Saturn [47], Uranus and [25] and Neptune [26]. It is a key ingredient in how researchers nowadays predict where reconnection may occur at the magnetopause for a given upstream IMF orientation [48]. Very recently, the same analytical approach has been undertaken with more realistic boundary geometries but still without coupling to the flow [51] and compared to THEMIS observations [50].

The magnetic field connectivity in the magnetosheath is reconstructed in three dimensions from our massive magnetosheath catalog. The details of the reconstruction of continuous field lines from discrete scattered in-situ measurements can be found in the method section. In the magnetostatic model, the magnetopause is assumed to be axisymmetric and represents an impenetrable boundary to which the magnetic field must be tangential. Under such conditions, the structure of the draping only depends on the absolute value of the IMF cone angle ( $\tan \theta_{co} = \sqrt{B_y^2 + B_z^2}/B_x$ ). The IMF clock angle ( $\tan \theta_{cl} = B_y/B_z$ ) just rotates the pattern around the Sun-Earth axis. In reality, the magnetopause can be crossed by field lines when magnetic reconnection occurs, which depends on the IMF clock angle. This may marginally impact the draping close to the boundary. An effect that we neglect in the present discussion by considering all IMF clock angles together. In the following, the data will thus adequately

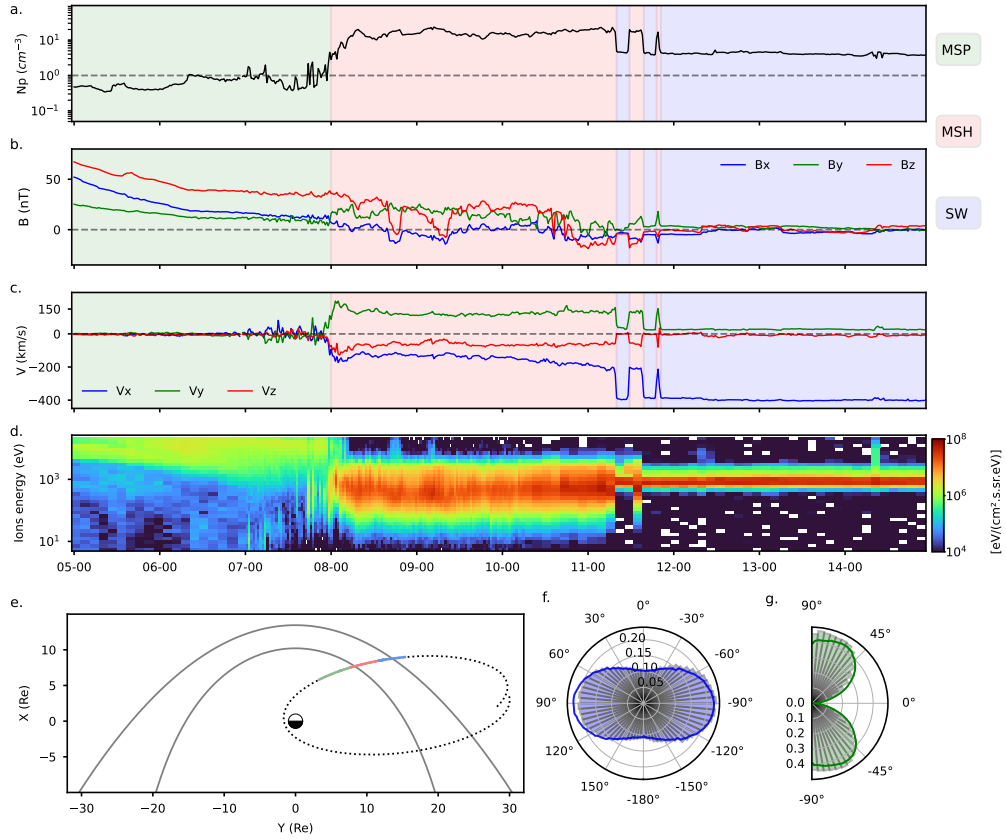


Figure 1: **In-situ data and orbit from THEMIS B probe on May 16 2008.** Panels **a** to **d** show respectively the ion density, the magnetic field components, the velocity components, the omnidirectional energy fluxes of ions. Panel **e** shows in the orbit of the probe on a 5-day period with the dotted line. The bow shock [11] and magnetopause [45] are represented as solid gray lines. In **a-c** and **e**, the green, red, and blue color filling and line colors correspond to the time intervals automatically classified by the machine learning algorithm as magnetosphere, magnetosheath and solar wind respectively. The blue and green histograms in **f** and **g** correspond to the polar density distribution of the IMF clock and cone angle, respectively, for all times associated with magnetosheath measurements. The blue and green solid lines represent the same distributions but for the whole twenty-six years of OMNI data.

be represented in the SWI coordinate system, as described in the method section. The following analysis thus focuses on specific sectors of the IMF cone angle.

The first comparison, shown in Fig 2, is made for large IMF cone angles within the range  $70^\circ \leq |\theta_{co}| \leq 80^\circ$ . At such a large cone angle, the IMF is almost perpendicular to the Sun-Earth axis, as can be seen in the two leftmost panels, representing the system in the plane containing the IMF. Note that although the magnetopause and the bow shock are represented by their cross-section in the  $X_{swi} - Y_{swi}$  plane, the magnetic field lines are the projection on that plane of lines exploring the three dimensions of space. Although small, the radial component of the magnetic field is sufficient to break the symmetry between the two sides of  $Y_{swi} = 0$ . The side where the IMF is most parallel to the shock surface normal vector, the so-called quasi-parallel side is found where  $Y_{swi} < 0$ , by convention of the SWI coordinate system adopted here. Respectively, the so-called quasi-perpendicular side is found for  $Y_{swi} > 0$ . By convention of the SWI system also, the  $X_{swi}$  component of the IMF is taken positive.

A quick glance at Fig. 2 reveals that the draping obtained with the magnetostatic model (upper panels **a,b,c**) is strikingly similar to the one obtained from in-situ data (lower panels **d,e,f**). The leftmost panels show that field lines in the quasi-perpendicular side exit the magnetosheath through the bow shock on the quasi-parallel side. The closer a line is from the magnetopause in the quasi-perpendicular side, the farther from the subsolar region it exits to the interplanetary medium. Consistently, the  $B_x$  component, positive in the quasi-perpendicular side, goes through zero around the subsolar region and becomes negative in the quasi-parallel region. The lines that appear to cross the magnetopause actually do not, but rise in the third dimension, above the  $Z_{swi} = 0$  plane to circumvent the magnetopause. This is better seen from the middle panels which represent the field lines close to the magnetopause surface as seen from the Sun vantage point. Initially contained in the  $X_{swi} - Y_{swi}$  plane upstream of the bow shock, the field lines bend in the  $Z_{swi}$  direction to wrap the magnetopause. The rightmost panels offer a complementary 3D view of the field lines close to the magnetopause. The great similarity between the modeled draping and the one obtained from in-situ data hides the fundamentally different underlying physical constraints they must satisfy. When considered, these constraints explain the subtle differences seen in this large IMF cone angle limit between lower and upper panels of Fig 2, and are at the root of a much more pronounced disagreement between the two draping patterns at lower cone angles, as will be explained in the following.

In the model (resp. the data), field lines must meet the imposed IMF orientation at the bow shock and must be exactly (resp. almost) tangential to the magnetopause. In the magnetostatic case where no electrical current flows within the magnetosheath volume, the magnetic field lines wrap the magnetopause like paper wraps a candy and diverge from two singular points at the magnetopause along the normal to the shock where it is parallel to the IMF. Without any other constraint, field lines just diverge away from these two singularities as prescribed by the magnetic potential function. This behavior explains the convergence of the field lines easily seen on the two flanks if looked at from the Sun standpoint in panel b of Fig. 2. In a perfect  $90^\circ$  IMF cone angle condition, the two singularities would be perfectly symmetric with respect to  $Y_{swi} = 0$ . Here, however, the singularity in the quasi-parallel region is closer to the subsolar region due to the slight radial component, resulting in slightly more pronounced apparent convergence of the field lines in the quasi-parallel region of Fig 2b.

In contrast, field lines in reality must also comply with the frozen-in condition, imposing that magnetically connected solar wind fluid elements must remain so during the draping. The temporal aspect of the draping then becomes important, and in the large IMF cone angle limit, follows the schematics of Figure 3a. Among the represented connected points, the red one is the first to meet the shock surface. In the subsolar region, that element will be strongly decelerated while other connected points remain in motion at the solar wind speed. Because the IMF cone angle is large, connected fluid elements are not far apart from one another along the Sun-Earth axis. The element arrived at the shock in the subsolar region (red dot) is thus still lagging in the slow stagnation flow region when other connected elements make contact with the shock. Together with the curved shape of the magnetopause and shock, this gives the observed bow shape to the field line, reminiscent of the one obtained in the magnetostatic model. Field lines close to the magnetopause are deflected around it and thus also bend in the Z directions like in the model, as seen from the Sun vantage point in Fig 2e. Coincidentally, field lines appear to converge more on the quasi-parallel side than in the quasi-perpendicular side as in the modeled draping. However, the reason here has nothing to do with topological singularities but is again found in the temporal sequence of the draping. Parts of the field lines that crossed the shock in the quasi-perpendicular region did so earlier than those in the quasi-parallel side. Consequently, they had more time to rise away from the  $Z_{swi} = 0$  plane and are thus found slightly more spread apart than their counterparts in the quasi-parallel side, but in a way that is slightly different than for the modeled field.

Differences between the model and data become more drastic as the IMF cone angle decreases. As it does so,

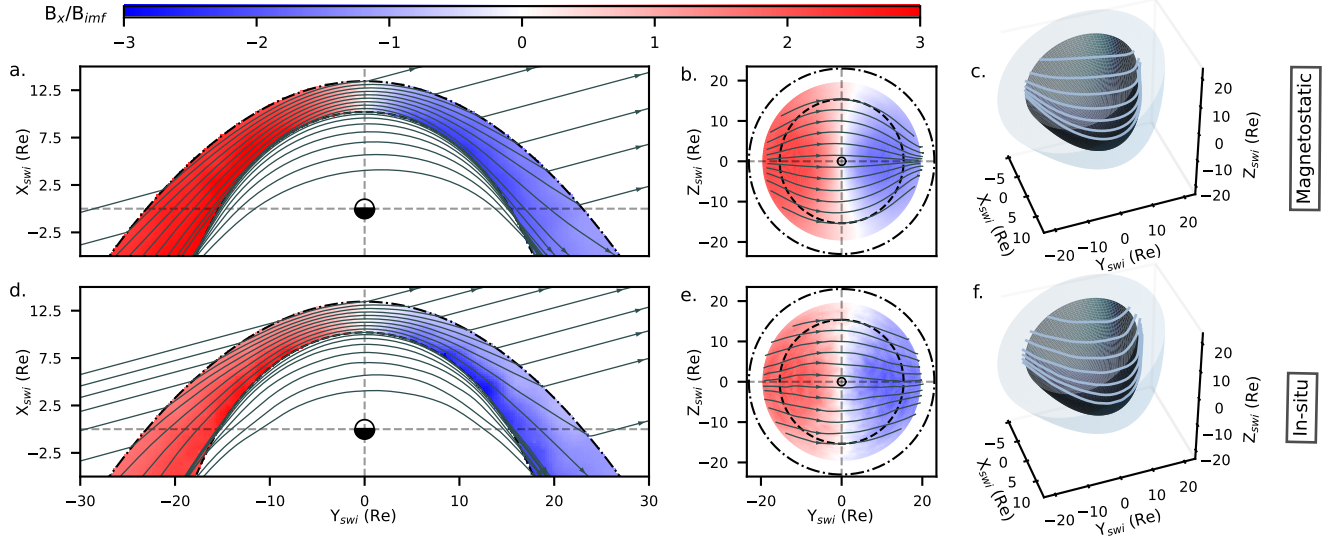


Figure 2: **Large IMF cone angle draping.** Subset  $70^\circ \leq |\theta_{co}| \leq 80^\circ$ . Panels **a-c** to and **d-f** correspond respectively to magnetostatic [22] and in-situ magnetic field. The color maps correspond to  $B_x/B_{imf}$ . The grey arrowed lines correspond to the magnetic field lines integrated in 3D (see the method section). Panels **a** and **d** correspond to the data close to the  $Z_{swi} = 0$  plane. Panels **b** and **e** correspond to the data close to the magnetopause [45]. The three-dimension views **c** and **f** show the magnetic field lines close to the magnetopause.

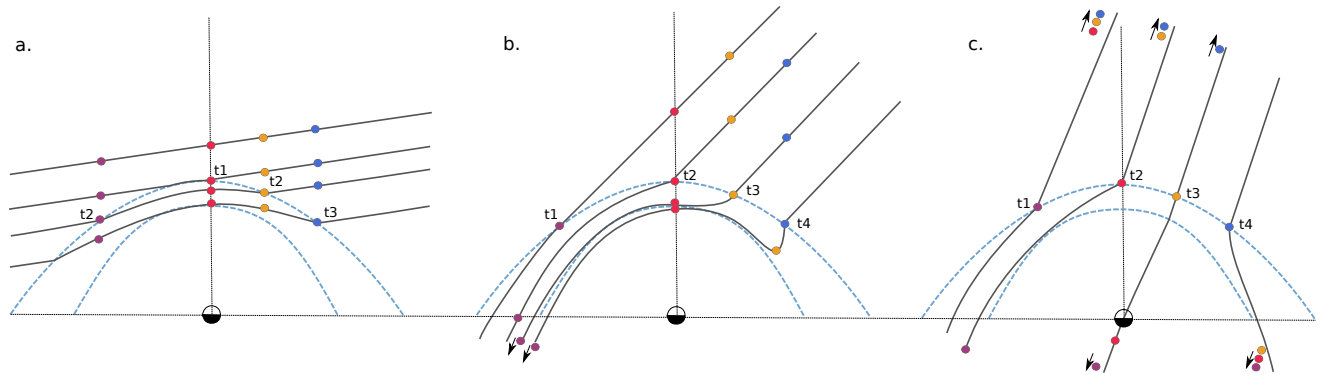


Figure 3: **Schematics of the draping mechanism.** Panels **a**, **b** and **c** represent the expected draping pattern for the large, intermediate and low IMF cone angle regimes, respectively.  $t_1$  to  $t_4$  represent the arrival time at the bow shock of the different fluid elements (purple, red, orange and blue points) connected by the same magnetic field line.

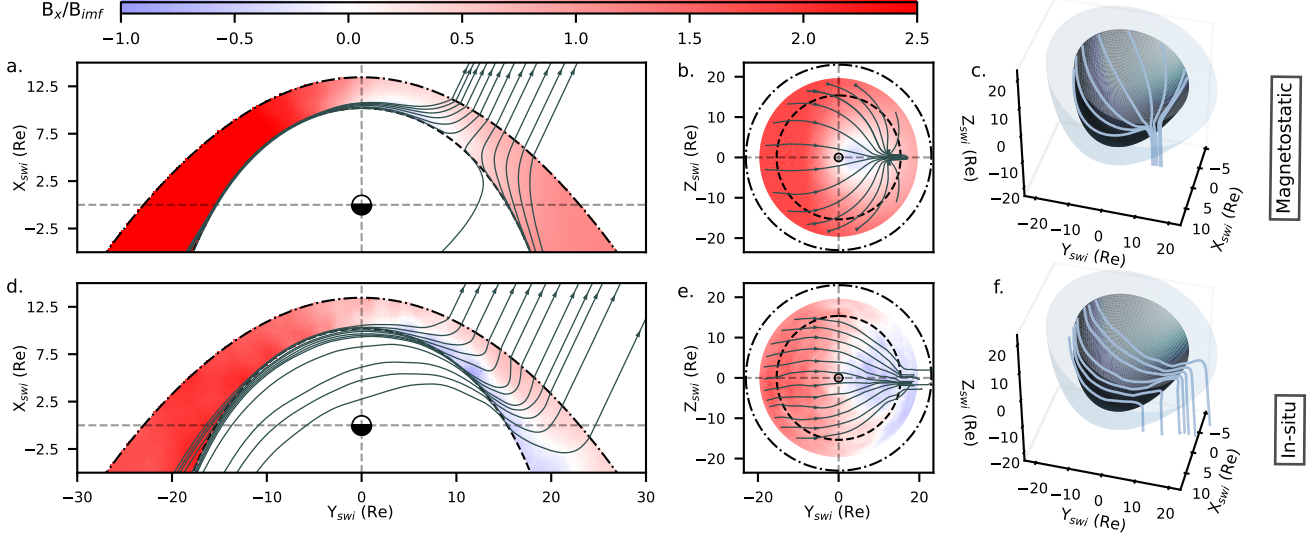


Figure 4: **Intermediate IMF cone angle draping.** Subset  $20^\circ \leq |\theta_{co}| \leq 30^\circ$ . The legend is the same as Fig 2.

the parallel shock region moves closer to the subsolar region. The previously discussed magnetic singularity of the model is now found closer to the subsolar region as well, as seen in Figure 4a. Clearly, this singularity is not seen in the data of panel d. In contrast, all the field lines obtained from in-situ data, no matter how far from subsolar region on the quasi-parallel side, eventually connect to more sunward regions, as reveals Fig 4d. Consequently,  $B_x$  takes negative values all along the magnetopause on the quasi-parallel side, exactly as it did for large IMF cone angles, and thus opposed to what the model predicts. This important difference again lies in the frozen-in condition constraining the draping pattern in reality.

As before, the part of the field line entered in the subsolar region does not have the time to re-accelerate before other parts arrive at the shock in the quasi-parallel region. Field lines entering the quasi-parallel region must thus again connect to the subsolar region. It is interesting to note, however, that the field lines do not immediately turn towards the dayside as soon as they cross the shock as they do for the large IMF cone angle regime. The key is that for lower IMF cone angle, connected elements are now further apart along  $X_{swi}$  in the solar wind, as can be seen on Fig. 3b. They are close enough for the subsolar part of the line to still lag behind by the time they arrive at the shock. However they are too far apart for elements entering the magnetosheath at any point of the quasi-parallel region to pass ahead of connected elements previously entered, as in the large cone angle regime. Upon crossing the bow shock in the quasi-parallel region, field lines thus must continue nightward over some distance before turning back towards the dayside. The sign of  $B_x$  is thus necessarily reversed across the magnetosheath in the quasi-parallel side, and an associated steady current sheet exists in the central magnetosheath over a significant portion of the dayside. This electrical current in the magnetosheath volume is the consequence of the frozen in condition only.

As previously noticed in the regime of large IMF cone angles (Fig 2b,e), an asymmetry is visible in the orientation of field lines between the quasi-parallel/perpendicular sides of the magnetosheath as viewed from the Sun (Fig 4b,e). However, here the asymmetry is much more pronounced (Fig 4b). In the modeled draping, this strong asymmetry simply relates to the singularity being now located closer to the subsolar region, towards which field lines must converge. In reality, the asymmetry still relates to the temporal aspect of the draping. For these lower IMF cone angles, connected fluid elements are more separated along  $X_{swi}$ . The delay between their arrival at the shock in the quasi-parallel and quasi-perpendicular is thus significantly longer. As a result, field lines in the quasi-perpendicular region have a much longer time to leave the plane  $Z = 0$ , but they need to remain connected to parts arrived near  $Z_{swi} = 0$ , leading to the observed asymmetry. The 3D plots on the rightmost panels offer a clear complementary overview of the fundamental difference between the two draping patterns.

An important question at this point is to what extent the model and data keep exhibiting these distinct topologies as the IMF cone angle decreases even further down to zero. For symmetry reasons, it is clear that for an exactly radial IMF, field lines must spread equally around from the subsolar point. In both the model and data  $\theta_{co} = 0$  must thus lead to a null point in that region, as it does only for the model for other IMF orientations on the

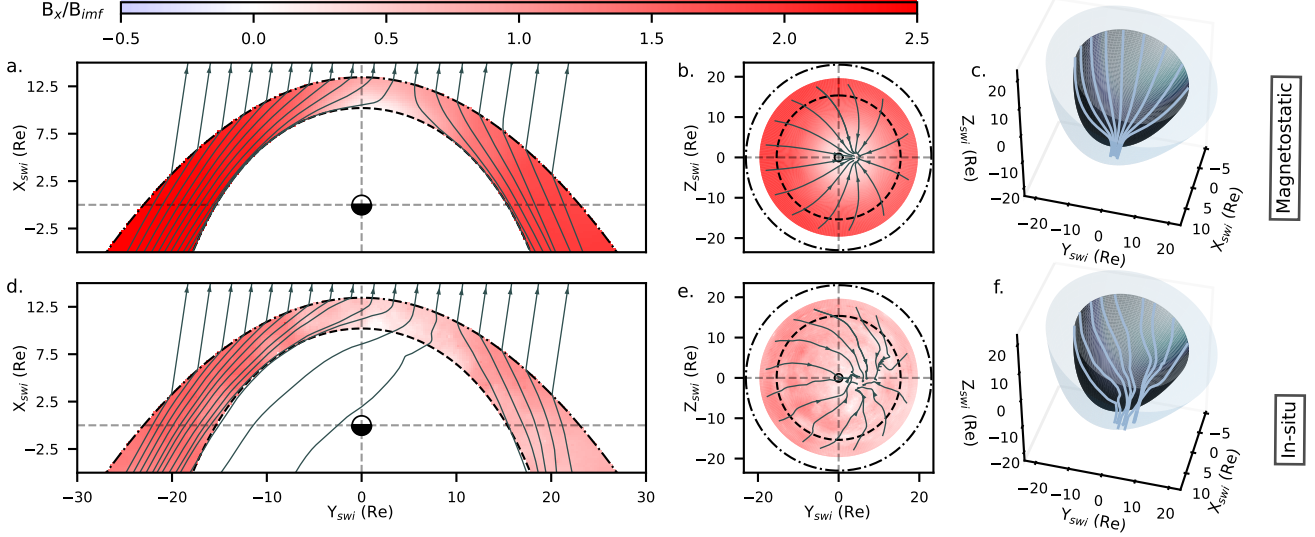


Figure 5: **Small IMF cone angle draping.** Subset  $0^\circ \leq |\theta_{co}| \leq 12.5^\circ$ . The legend is the same as Fig 2.

quasi-parallel side. It is unclear at this point, however, whether data only shows this divergent pattern for the null cone angle or not.

The answer is clearly seen on Fig 5, which represents both modeled and observed draping for a very small but non-zero IMF cone angle. In that regime, it is unsurprising to see that the modeled draping only differs from previous ones by the position of the magnetic singularity, now much closer to the subsolar point. It is, however, interesting to notice that the observed draping now also exhibits a similar structure, with an apparent divergence of the field lines originating approximately from the same location as in the model.

The pattern obtained with data within this low IMF cone angle regime is very noisy, due to the limited amount of data (Fig 1g) and the likely presence of enhanced fluctuations in that region downstream of the foreshock. However, the results appear again consistent with the dominant effect of the frozen-in condition, and in particular with the temporal aspect of the draping, represented in the rightmost panel of Fig. 3. For such a low yet non-zero IMF cone angle, connected fluid elements are now so far from each other along  $X_{swi}$  that their arrival time at the shock is significantly longer than the time it takes for the red element to leave the flow stagnation region. The part of the field line entering the subsolar region thus no longer acts as a bottleneck as it did for the two preceding regimes. Fluid elements arriving at the shock in the quasi-parallel region are now connected to elements that have traveled a long distance in the magnetosheath and are located much more nightward. As a result, the draping pattern is again close to the one obtained in the model, since like in the large cone angle regime, the frozen-in condition does not lead to the existence of a current sheet in the magnetosheath volume, which the model ignores.

Although model and data broadly agree again in this very low IMF cone angle regime, some subtle differences still reveal the underlying role of the frozen-in condition in data. The field lines obtained from in-situ data (Fig 5d) in the quasi-parallel region indeed appear to come back towards the magnetopause, consistently with the idea that they should, for some time at least, still remain connected to their previously entered counterpart in the quasi-perpendicular side. In contrast, the magnetostatic field lines (Fig 5a), ignoring the frozen-in constraint, have a completely uncorrelated behavior on both side of the singularity.

Previous figures gave us a qualitative and consistent picture of the importance of the frozen-in condition for understanding the structure of the field line draping around the magnetopause. The following analysis now tests this interpretation in a more quantitative way. We focus on Fig. 6, where each panel represents the dayside magnetosphere in the  $X_{swi} - Y_{swi}$  plane for each of the three draping regimes previously identified. Each panel shows green and red magnetic field lines, obtained from the magnetostatic model and in-situ data, respectively, and flow stream lines obtained from in-situ data as well. Each line is again the result of a three-dimensional integration. The red and green magnetic field lines are chosen to intersect the bow shock at an arbitrary but identical position, located in the quasi-parallel side of the system. Knowing the point at which the magnetic field line intersects the bow shock, the IMF cone angle, and given a solar wind velocity assumed steady, it is easy to compute the time delay

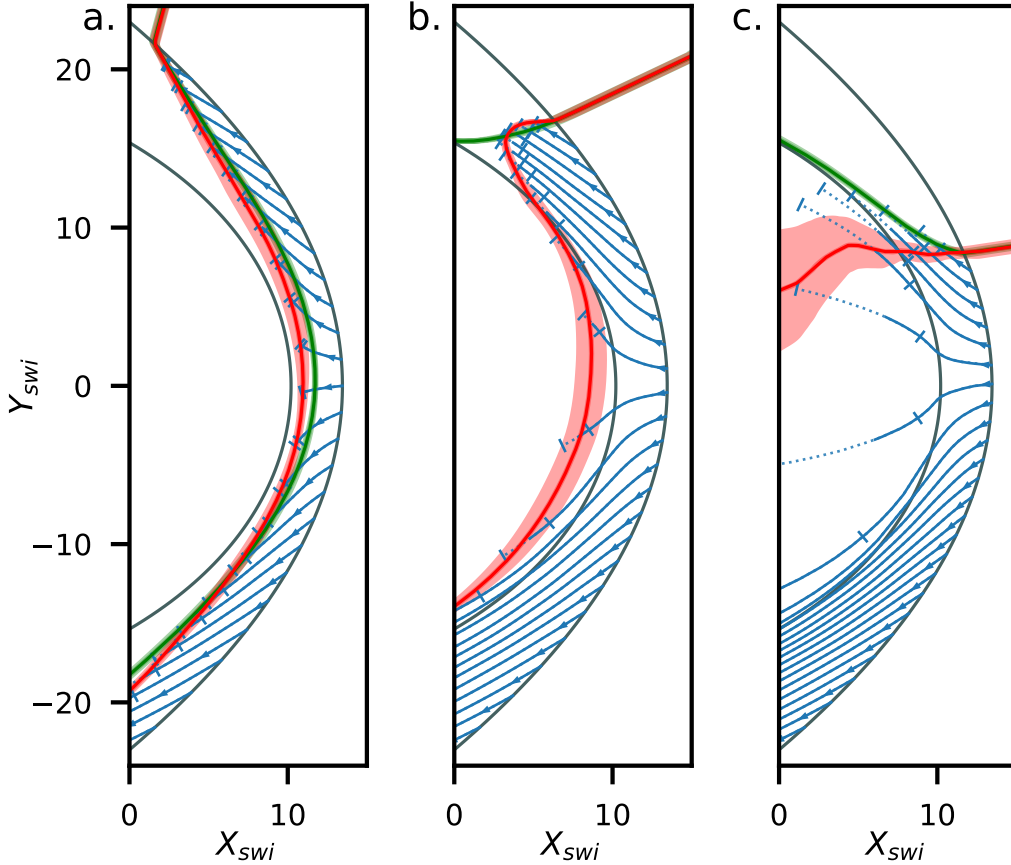


Figure 6: **Quantitative estimate of the flux freezing condition.** Panels **a**, **b** and **c** are associated with the large, intermediate and low IMF cone angle regimes, respectively. The red and green lines represent the magnetic field lines obtained from in-situ data and the magnetostatic model [21], respectively. The uncertainty on the position of the field lines is represented with the shaded area and is calculated with the integration of 1500 field lines with starting points in a sphere of  $0.5 R_e$  of diameter. The solid blue lines correspond to the plasma streamlines integrated in 3D with in-situ measurements of the velocity (see method). The error bars are determined for each line by calculating the integration times (see method) corresponding to the first and third quartile of the distribution of the IMF cone angle in each subset.

between the time of the representation and that at which the field line crossed the bow shock at any other point. Multiple points are thus chosen on the bow shock as starting points of flow lines. 3D flow lines, integrated during the time delay associated to their starting point, stop right on top of the magnetic field line obtained from data for the large and intermediate IMF cone angle regimes (Fig 6a,b). The agreement is remarkable, considering that the integration time only assumes a constant solar wind velocity, a steady IMF orientation, and given that the magnetic field and velocity are two independent in-situ measurements. The flow line integration also agrees better with the magnetic field data than with that of the model in the large cone angle one, despite their very close behavior. This analysis clearly confirms previous qualitative interpretations in each of the IMF cone angle regimes. In the very IMF low cone angle limit (Fig 6c), the results remain consistent, even if the scarcity of the data increases a lot the uncertainty associated with the field line integration. In addition the large delay between arrival times at the shock leaves room for many processes to invalidate the steady state assumption our study is based on. Furthermore, it is not clear to what extent fluid elements arriving at the shock remain connected to nightside regions for such long times.

It has been known for decades that the interplanetary magnetic field drapes around the magnetosphere of the Earth as it crosses the bow shock. In-situ evidences for the draping have, however, so far been very local. Only

Mission	Probe	Period	Instruments
Cluster	C1	2001-2019	Cluster Ion Spectrometry (CIS) [38]
	C3	2001-2009	Fluxgate Magnetometer (FGM) [2]
DoubleStar	TC1	2004-2007	Hot Ion Analyzer (HIA) [39] Fluxgate Magnetometer (FGM) [5]
Themis	P3, P4, P5	2007-2021	Electrostatic Analyzers (ESA) [29]
	P1, P2	2007-2009	Fluxgate Magnetometer (FGM) [1]
Magnetospheric Multiscale	MMS1	2015-2021	Plasma Investigation (FPI) [36] Fluxgate Magnetometer (FGM) [41]

Table 1: **Source of the in-situ data.**

global magnetohydrodynamics numerical models have provided a complete, global and three-dimensional structure of the draping for a given IMF orientation. Through the use of innovative machine learning based in-situ detection and modeling, this study is the first to offer such a global view from a purely observational standpoint. For large ( $|\theta_{co}| > 45^\circ \pm 5^\circ$ ) or extremely small ( $12.5^\circ \pm 2.5^\circ < |\theta_{co}|$ ) IMF cone angles, the global draping is found to be qualitatively consistent with a magnetostatic draping assuming no current in the magnetosheath volume [22]. In contrast, data clearly and fundamentally disagree with the magnetostatic draping in the intermediate cone angle regime ( $12.5^\circ \pm 2.5^\circ < |\theta_{co}| < 45.0^\circ \pm 5^\circ$ ) and angular deviations can be as high as about  $180^\circ$  in some portions of the quasi-parallel magnetosheath. In the data, field lines fold onto the magnetopause surface and are constrained to remain frozen in solar wind fluid elements. This folding is associated to a large scale current sheet at mid-depth in the quasi-parallel magnetosheath. This scenario is further quantitatively validated by mapping magnetic field lines with the 3D integration of the independently measured flow velocity. The detailed structure of the magnetic field draping, shown in our study to be intrinsically linked to the radial flow of the magnetosheath plasma, constitutes the immediate boundary condition for the magnetosphere system. It is in particular relevant to where magnetic reconnection occurs and operate, and thus how the Earth system couples to its environment. Our study also shows how having decades of data from multiple missions enables the assessment of global yet detailed and quantitative properties of the Earth magnetosphere despite the fundamentally local character of in-situ measurements. Although considerably less data exists, these results are also relevant to the case of other planets and obstacles to magnetized plasma flows.

## 1 Methods

### Satellites and instrumentation

The in-situ data are provided by the instruments of the four missions shown in Table 1. The data are resampled to a 5s resolution, on which a 3 points median filter is applied to remove outliers.

### Selection of magnetosheath data

The plasma moments and magnetic field were used to automatically identify [30] the magnetosheath dataset with a gradient boosting algorithm [33]. A perfect forecast obtains an Heidke Skill Score (HSS) and Area Under Curve (AUC) score of 1. Our classification is highly effective considering that it obtains average values of 0.980 and 0.998 for each score respectively. The data with density lower than  $4cm^{-3}$  has been removed to discard the majority of the magnetopause boundary layer crossings. More than 50 millions of magnetosheath in-situ measurements have been automatically selected. The aberration on the velocity due to the orbital motion of the Earth has been corrected.

### Solar wind parameters

Each magnetosheath data point is associated to solar wind and IMF properties (magnetic field, density, temperature, velocity, dynamic pressure, Mach number, plasma beta) from the OMNI dataset [20] measured at a previous time. This time delay is associated with the propagation of the IMF between the nose of the bow at which OMNI data is defined and the spacecraft position. The time delay is estimated using the propagation method of Safrankova et al. 2002 [42].

## Boundaries models with Machine learning

The measurement’s relative positions to the magnetopause and bow shock must be found to calculate the magnetostatic field and to normalize their location between average boundaries. The Gradient Boosting Regressor (GBR) [33] algorithm was used to predict the position of the boundaries given the solar wind parameters and tilt angle. To proceed, 33563 magnetopause and 19361 bow shock single crossings on 10 minutes windows have been identified using the Nguyen et al. 2021 [30] method. Crossings in a solid angle of  $7.5^\circ$  and at less than 30 minutes of each others are considered as partial crossings and are therefore grouped together to ensure the independence of the train/test sets. A cross-validation has been performed with a 90/10 split between those two sets and a Root Mean Square Error (RMSE) of  $0.78 \pm 0.03$  Re for the magnetopause model and of  $0.96 \pm 0.06$  Re for the bow shock model have been obtained.

## Magnetic field model computation

The magnetostatic model for Kobel and Fluckiger 1994 [22] is calculated for each measured point in our magnetosheath dataset, using the regression models of the magnetopause and bow shock transformed into parabolic and confocal approximation.

## Spatial representation of the dataset

First, it should be noticed that the same methodology has been used to build the spatial representation of the draping, regardless of the origin of the magnetic field value (model or data). The GSM positions have been normalized between the average models of Shue et al. 1998 [45] and Jelinek et al. 2012 [11] using the relative positions to the machine learning boundaries models given the solar wind conditions of each point. The points located too far outside the magnetosheath as predicted by the boundaries models have been excluded, bringing the total number of data in this study to almost 45 million measurements.

The solar wind interplanetary (SWI) magnetic field coordinate system [53] is used in this study. This system depends on the magnetic field and velocity of the solar wind. The  $X_{swi}$  axis is colinear to the solar wind velocity vector and points towards the sun. The magnetic field vector expressed in the SWI coordinate system only has components along the  $X_{swi}$  and  $Y_{swi}$  axis.  $B_{imf}$  is furthermore transformed to have  $B_{ximf}$  positive so that draping pattern is invariant.

Each point of the colormaps is the result of weighted average over the  $k$  nearest samples using the KNeighborsRegressor [33] algorithm.

## Integration of the magnetic field and flow lines

The magnetic and velocity field lines have been integrated in 3D with `solv_ivp` [52], where the magnetic field at each integration step is provided by the KNeighborsRegressor [33] algorithm. The propagation time  $\Delta t$  of the flow lines in Figure 6 has been calculated with (1).

$$\Delta t = \frac{\frac{\Delta Y}{\tan \theta_{co}} + \Delta X_{bs}}{V_{sw}} \quad (1)$$

$\Delta Y$  is the distance along the Y axis between the start points at the bow shock of the magnetic field and flow lines,  $\Delta X_{bs}$  is the distance along the X axis between those start points produced by the bow shock shape,  $\theta_{co}$  is the cone angle and  $V_{sw}$  is the solar wind velocity.

## Data availability

The in-situ data are available by using the Speasy package (<https://github.com/SciQLop/speasy>). It allows to access the data on the CDAweb database (<https://cdaweb.gsfc.nasa.gov>) for the THEMIS mission, and AMDA database (<http://amda.irap.omp.eu>) for Cluster, DoubleStar, and MMS missions.

## Code availability

The code to reproduce the figures is available on <https://github.com/BayaneMdW/drapingmsh.git>.

## 2 Bibliography

### References

- [1] H. U. Auster, K. H. Glassmeier, W. Magnes, O. Aydogar, W. Baumjohann, D. Constantinescu, D. Fischer, K. H. Fornacon, E. Georgescu, P. Harvey, O. Hillenmaier, R. Kroth, M. Ludlam, Y. Narita, R. Nakamura, K. Okrafka, F. Plaschke, I. Richter, H. Schwarzl, B. Stoll, A. Valavanoglou, and M. Wiedemann. The THEMIS Fluxgate Magnetometer. *Scientific Studies of Reading*, 141(1-4):235–264, Dec 2008.
- [2] Andre Balogh, C. Carr, Melina Acuña, M. Dunlop, T. Beek, P. Brown, K.-H Fornacon, E. Georgescu, K.-H Glassmeier, J. Harris, G. Musmann, Timothy Oddy, and Konrad Schwingenschuh. The cluster magnetic field investigation: Overview of in-flight performance and initial results. *Annales Geophysicae*, 19, 10 2001.
- [3] Kenneth W. Behannon and Donald H. Fairfield. Spatial variations of the magnetosheath magnetic field. *Planetary and Space Science*, 17(10):1803–1816, 1969.
- [4] C Bertucci, F Duru, N Edberg, M Fraenz, C Martinecz, K Szego, and O Vaisberg. The Induced Magnetospheres of Mars, Venus, and Titan. *Space Science Reviews*, 162(1-4):113–171, 2011.
- [5] C. Carr, P. Brown, T. L. Zhang, J. Gloag, T. Horbury, E. Lucek, W. Magnes, H. O’Brien, T. Oddy, U. Auster, P. Austin, O. Aydogar, A. Balogh, W. Baumjohann, T. Beek, H. Eichelberger, K. H. Fornacon, E. Georgescu, K. H. Glassmeier, M. Ludlam, R. Nakamura, and I. Richter. The Double Star magnetic field investigation: instrument design, performance and highlights of the first year’s observations. *Annales Geophysicae*, 23(8):2713–2732, Nov 2005.
- [6] I J Coleman. A multi-spacecraft survey of magnetic field line draping in the dayside magnetosheath. *Annales Geophysicae*, 23(3):885 – 900, 03 2005.
- [7] N U Crooker, J. G. Luhmann, C. Russell, E J Smith, J R Spreiter, and S S Stahara. Magnetic field draping against the dayside magnetopause. *Journal of Geophysical Research (Space Physics)*, 90(A4):3505 – 3510, 04 1985.
- [8] M. Delva, M. Volwerk, R. Jarvinen, and C. Bertucci. Asymmetries in the Magnetosheath Field Draping on Venus’ Nightside. *Journal of Geophysical Research: Space Physics*, 122(10):10,396–10,407, 2017.
- [9] D. H. Fairfield. *The ordered magnetic field of the magnetosheath*, volume 72 of *Journal of Geophysical Research*. 00 1967.
- [10] V. Génot, L. Broussillou, E. Budnik, P Hellinger, P M Trávníček, E. Lucek, and I. Dandouras. Timing mirror structures observed by Cluster with a magnetosheath flow model. *Annales Geophysicae*, 29(1):1849 – 1860, 10 2011.
- [11] K. Jelínek, Z. Němeček, and J. Šafránková. A new approach to magnetopause and bow shock modeling based on automated region identification. *Journal of Geophysical Research (Space Physics)*, 117(A5):A05208, May 2012.
- [12] G. H. Jones, A. Rees, A. Balogh, and R. J. Forsyth. The draping of heliospheric magnetic fields upstream of coronal mass ejecta. *Geophysical Research Letters*, 29(11):15–1–15–4, 2002.
- [13] Antal Juhász and Mihály Horányi. Dynamics of charged space debris in the Earth’s plasma environment. *Journal of Geophysical Research: Space Physics*, 102(A4):7237–7246, 1997.
- [14] Antal Juhász and Mihály Horányi. Magnetospheric screening of cosmic dust. *Journal of Geophysical Research: Space Physics*, 104(A6):12577–12583, 1999.
- [15] Esa J. Kallio and Hannu E. J. Koskinen. A semiempirical magnetosheath model to analyze the solar wind-magnetosphere interaction. , 105(A12):27469–27480, December 2000.
- [16] Z Kaymaz. IMP 8 magnetosheath field comparisons with models. *Annales Geophysicae*, 16(4):376 – 387, 04 1998.

- [17] Z Kaymaz, J. G. Luhmann, J A Fedder, J G Lyon, J R Spreiter, and S S Stahara. Evidence for reverse draping of magnetosheath field around the magnetosphere in IMP 8 observations for northward interplanetary magnetic field. *Journal of Geophysical Research (Space Physics)*, 101(A6):13321 – 13326, 06 1996.
- [18] Zerefsan Kaymaz, George Siscoe, and Janet G Luhmann. IMF draping around the Geotail: IMP 8 observations. *Geophysical Research Letters*, 19(8):829–832, 1992.
- [19] Zerefsan Kaymaz and George Siscoe. Field-Line Draping Around ICMES. *Solar Physics*, 239(1-2):437–448, 2006.
- [20] J. H. King and N. E. Papitashvili. Solar wind spatial scales in and comparisons of hourly Wind and ACE plasma and magnetic field data. *Journal of Geophysical Research (Space Physics)*, 110(A2):A02104, February 2005.
- [21] E Kobel and E O Fluckiger. A model of the steady state magnetic field in the magnetosheath. *Journal of Geophysical Research (ISSN 0148-0227)*, 99(A12):23, 12 1994.
- [22] E. Kobel and E. O. Fluckiger. A model of the steady state magnetic field in the magnetosheath. , 99(A12):23617–23622, December 1994.
- [23] C. Koenders, C. Goetz, I. Richter, U. Motschmann, and K.-H. Glassmeier. Magnetic field pile-up and draping at intermediately active comets: results from comet 67P/Churyumov–Gerasimenko at 2.0 AU. *Monthly Notices of the Royal Astronomical Society*, 462(Suppl.1):S235–S241, 2016.
- [24] M Longmore, S.. Schwartz, and E.. Lucek. Rotation of the magnetic field in Earth’s magnetosheath by bulk magnetosheath plasma flow. *Annales Geophysicae*, 24(1):339 – 354, 03 2006.
- [25] A Masters. Magnetic reconnection at Uranus’ magnetopause. *Journal of Geophysical Research: Space Physics*, 119(7):5520–5538, 2014.
- [26] A. Masters. Magnetic reconnection at Neptune’s magnetopause. *Journal of Geophysical Research: Space Physics*, 120(1):479–493, 2015.
- [27] A Masters. Model-Based Assessments of Magnetic Reconnection and Kelvin-Helmholtz Instability at Jupiter’s Magnetopause. *Journal of Geophysical Research (Space Physics)*, 122(1):11, 11 2017.
- [28] D. J. McComas, J. T. Gosling, D. Winterhalter, and E. J. Smith. Interplanetary magnetic field draping about fast coronal mass ejecta in the outer heliosphere. *Journal of Geophysical Research: Space Physics*, 93(A4):2519–2526, 1988.
- [29] J. P. McFadden, C. W. Carlson, D. Larson, M. Ludlam, R. Abiad, B. Elliott, P. Turin, M. Marckwordt, and V. Angelopoulos. The THEMIS ESA Plasma Instrument and In-flight Calibration. *Scientific Studies of Reading*, 141(1-4):277–302, Dec 2008.
- [30] G. Nguyen, N. Aunai, B. Michotte de Welle, A. Jeandet, B. Lavraud, and D. Fontaine. Massive Multi-Mission Statistical Study and Analytical Modeling of the Earth’s Magnetopause: 1. A Gradient Boosting Based Automatic Detection of Near-Earth Regions. *Journal of Geophysical Research: Space Physics*, 127(1), 2022.
- [31] S Kokubun S Ohtani and kokubun. Magnetic properties of the high-latitude tail boundary: Draping of magnetosheath field lines and tail-aligned current. 96(A6):1 – 10, 1991.
- [32] M. Opher, E. C. Stone, and T. I. Gombosi. The Orientation of the Local Interstellar Magnetic Field. *Science*, 316(5826):875–878, 2007.
- [33] F. Pedregosa, G. Varoquaux, A. Gramfort, V. Michel, B. Thirion, O. Grisel, M. Blondel, P. Prettenhofer, R. Weiss, V. Dubourg, J. Vanderplas, A. Passos, D. Cournapeau, M. Brucher, M. Perrot, and E. Duchesnay. Scikit-learn: Machine learning in Python. *Journal of Machine Learning Research*, 12:2825–2830, 2011.
- [34] Christoph Pfrommer and Jonathan Dursi. Detecting the orientation of magnetic fields in galaxy clusters. *Nature Physics*, 6(7):520–526, 2010.

- [35] N. V. Pogorelov, F. Fraternali, T. K. Kim, L. F. Burlaga, and D. A. Gurnett. Magnetic Field Draping of the Heliopause and Its Consequences for Radio Emission in the Very Local Interstellar Medium. *The Astrophysical Journal Letters*, 917(2):L20, 2021.
- [36] C. Pollock, T. Moore, A. Jacques, J. Burch, U. Gliese, Y. Saito, T. Omoto, L. Avanov, A. Barrie, V. Coffey, J. Dorelli, D. Gershman, B. Giles, T. Rosnack, C. Salo, S. Yokota, M. Adrian, C. Aoustin, C. Auletta, S. Aung, V. Bigio, N. Cao, M. Chandler, D. Chornay, K. Christian, G. Clark, G. Collinson, T. Corris, A. De Los Santos, R. Devlin, T. Diaz, T. Dickerson, C. Dickson, A. Diekmann, F. Diggs, C. Duncan, A. Figueroa-Vinas, C. Firman, M. Freeman, N. Galassi, K. Garcia, G. Goodhart, D. Guererro, J. Hageman, J. Hanley, E. Hemminger, M. Holland, M. Hutchins, T. James, W. Jones, S. Kreisler, J. Kujawski, V. Lavu, J. Lobell, E. LeCompte, A. Lukemire, E. MacDonald, A. Mariano, T. Mukai, K. Narayanan, Q. Nguyen, M. Onizuka, W. Paterson, S. Persyn, B. Piepgrass, F. Cheney, A. Rager, T. Raghuram, A. Ramil, L. Reichenthal, H. Rodriguez, J. Rouzaud, A. Rucker, Y. Saito, M. Samara, J. A. Sauvaud, D. Schuster, M. Shappirio, K. Shelton, D. Sher, D. Smith, K. Smith, S. Smith, D. Steinfeld, R. Szymkiewicz, K. Tanimoto, J. Taylor, C. Tucker, K. Tull, A. Uhl, J. Vloet, P. Walpole, S. Weidner, D. White, G. Winkert, P. S. Yeh, and M. Zeuch. Fast Plasma Investigation for Magnetospheric Multiscale. *Scientific Studies of Reading*, 199(1-4):331–406, Mar 2016.
- [37] W. Reidler, K. Schwingenschuh, Ye. G. Yeroshenko, V. A. Styashkin, and C. T. Russell. Magnetic field observations in comet Halley’s coma. *Nature*, 321(Suppl 6067):288–289, 1986.
- [38] H. Rème, C. Aoustin, J. M. Bosqued, I. Dandouras, B. Lavraud, J. A. Sauvaud, A. Barthe, J. Bouyssou, Th. Camus, O. Coeur-Joly, A. Cros, J. Cuvilo, F. Ducay, Y. Garbarowitz, J. L. Medale, E. Penou, H. Perrier, D. Romefort, J. Rouzaud, C. Vallat, D. Alcaydé, C. Jacquy, C. Mazelle, C. D’Uston, E. Möbius, L. M. Kistler, K. Crocker, M. Granoff, C. Moukiss, M. Popecki, M. Vosbury, B. Klecker, D. Hovestadt, H. Kucharek, E. Kuenneth, G. Paschmann, M. Scholer, N. Scopke (), E. Seidenschwang, C. W. Carlson, D. W. Curtis, C. Ingraham, R. P. Lin, J. P. McFadden, G. K. Parks, T. Phan, V. Formisano, E. Amata, M. B. Bavassano-Cattaneo, P. Baldetti, R. Bruno, G. Chionchio, A. di Lellis, M. F. Marcucci, G. Pallochia, A. Korth, P. W. Daly, B. Graeve, H. Rosenbauer, V. Vasyliunas, M. McCarthy, M. Wilber, L. Eliasson, R. Lundin, S. Olsen, E. G. Shelley, S. Fuselier, A. G. Ghielmetti, W. Lennartsson, C. P. Escoubet, H. Balsiger, R. Friedel, J. B. Cao, R. A. Kovrazhkin, I. Papamastorakis, R. Pellat, J. Scudder, and B. Sonnerup. First multispacecraft ion measurements in and near the Earth’s magnetosphere with the identical Cluster ion spectrometry (CIS) experiment. *Annales Geophysicae*, 19:1303–1354, Oct 2001.
- [39] H. Rème, I. Dandouras, C. Aoustin, J. M. Bosqued, J. A. Sauvaud, C. Vallat, P. Escoubet, J. B. Cao, J. Shi, M. B. Bavassano-Cattaneo, G. K. Parks, C. W. Carlson, Z. Pu, B. Klecker, E. Moebius, L. Kistler, A. Korth, and R. Lundin. The HIA instrument on board the Tan Ce 1 Double Star near-equatorial spacecraft and its first results. *Annales Geophysicae*, 23(8):2757–2774, November 2005.
- [40] SM Petrinec Advances in Space Research. Draping of strongly flow-aligned interplanetary magnetic field about the magnetopause. *Advances in Space Research*, 2016.
- [41] C. T. Russell, B. J. Anderson, W. Baumjohann, K. R. Bromund, D. Dearborn, D. Fischer, G. Le, H. K. Leinweber, D. Leneman, W. Magnes, J. D. Means, M. B. Moldwin, R. Nakamura, D. Pierce, F. Plaschke, K. M. Rowe, J. A. Slavin, R. J. Strangeway, R. Torbert, C. Hagen, I. Jernej, A. Valavanoglou, and I. Richter. The Magnetospheric Multiscale Magnetometers. *Scientific Studies of Reading*, 199(1-4):189–256, Mar 2016.
- [42] J. Safránková, Z. Nemecek, S. Dusík, L. Prech, D. G. Sibeck, and N. N. Borodkova. The magnetopause shape and location: a comparison of the Interball and Geotail observations with models. *Annales Geophysicae*, 20(3):301–309, March 2002.
- [43] D. Schmid, Y. Narita, F. Plaschke, M. Volwerk, R. Nakamura, and W. Baumjohann. Pick-Up Ion Cyclotron Waves Around Mercury. *Geophysical Research Letters*, 48(9), 2021.
- [44] Daniel Schmid, Yasuhito Narita, Ferdinand Plaschke, Martin Volwerk, Rumi Nakamura, and Wolfgang Baumjohann. Magnetosheath plasma flow model around Mercury. *Annales Geophysicae*, 39(3):563–570, 2021.

- [45] J. H. Shue, P. Song, C. T. Russell, J. T. Steinberg, J. K. Chao, G. Zastenker, O. L. Vaisberg, S. Kokubun, H. J. Singer, T. R. Detman, and H. Kawano. Magnetopause location under extreme solar wind conditions. , 103(A8):17691–17700, August 1998.
- [46] John R. Spreiter, Audrey L. Summers, and Alberta Y. Alksne. Hydromagnetic flow around the magnetosphere. *Planetary and Space Science*, 14(3):223–253, 1966.
- [47] A H Sulaiman, A Masters, M K Dougherty, and X Jia. The magnetic structure of Saturn’s magnetosheath. *Journal of Geophysical Research (Space Physics)*, 119(7):5651 – 5661, 07 2014.
- [48] K J Trattner, S M Petrinec, and S.. Fuselier. The Location of Magnetic Reconnection at Earth’s Magnetopause. *Space Science Reviews*, 217(3):1 – 47, 04 2021.
- [49] L. Turc, D. Fontaine, P. Savoini, and E. K. J. Kilpua. A model of the magnetosheath magnetic field during magnetic clouds. *Annales Geophysicae*, 32(2):157–173, February 2014.
- [50] M Vandas, Z Nemecek, J Ā afránková, E P Romashets, and M Hajoš. Comparison of Observed and Modeled Magnetic Fields in the Earth’s Magnetosheath. *Journal of Geophysical Research (Space Physics)*, 125(3):e27705, 03 2020.
- [51] M Vandas and E P Romashets. Modeling of magnetic field in the magnetosheath using elliptic coordinates. *Planetary and Space Science*, 178:104692, 11 2019.
- [52] Pauli Virtanen, Ralf Gommers, Travis E. Oliphant, Matt Haberland, Tyler Reddy, David Cournapeau, Evgeni Burovski, Pearu Peterson, Warren Weckesser, Jonathan Bright, Stéfan J. van der Walt, Matthew Brett, Joshua Wilson, K. Jarrod Millman, Nikolay Mayorov, Andrew R. J. Nelson, Eric Jones, Robert Kern, Eric Larson, C J Carey, İlhan Polat, Yu Feng, Eric W. Moore, Jake VanderPlas, Denis Laxalde, Josef Perktold, Robert Cimrman, Ian Henriksen, E. A. Quintero, Charles R. Harris, Anne M. Archibald, Antônio H. Ribeiro, Fabian Pedregosa, Paul van Mulbregt, and SciPy 1.0 Contributors. SciPy 1.0: Fundamental Algorithms for Scientific Computing in Python. *Nature Methods*, 17:261–272, 2020.
- [53] Hui Zhang, Suiyan Fu, Zuyin Pu, Jianyong Lu, Jun Zhong, Changbo Zhu, Weixing Wan, and Libo Liu. Statistics on the Magnetosheath Properties Related to Magnetopause Magnetic Reconnection. , 880(2):122, August 2019.